Electron, Photon, and Neutron Dose Conversion Coefficients of Lens and Non-Lens Tissues Using a Multi-Tissue Eye Model to Assess Risk of Cataracts and Retinitis

Authors: Ali, Fawaz, and Richardson, Richard B.

Source: Radiation Research, 200(2) : 162-175

Published By: Radiation Research Society

URL: https://doi.org/10.1667/RADE-23-00023.1

RADIATION RESEARCH **200**, 162–175 (2023)
0033-7587/23 $15.00

DOI: 10.1667/RADE-23-00023.1

Electron, Photon, and Neutron Dose Conversion Coefficients of Lens and Non-Lens Tissues Using a Multi-Tissue Eye Model to Assess Risk of Cataracts and Retinitis

Fawaz Ali,[a] Richard B. Richardson[a,b,1]

[a] Canadian Nuclear Laboratories, Chalk River, Canada; [b] McGill University, Montreal, Canada

Ali F, Richardson RB. Electron, Photon, and Neutron Dose Conversion Coefficients of Lens and Non-Lens Tissues Using a Multi-Tissue Eye Model to Assess Risk of Cataracts and Retinitis. Radiat Res. 200, 162–175 (2023).

Previous publications describe the estimation of the dose from ionizing radiation to the whole lens or parts of it but have not considered other eye tissues that are implicated in cataract development; this is especially critical for low-dose, low-ionizing-density exposures. A recent review of the biological mechanisms of radiation-induced cataracts showed that lenticular oxidative stress can be increased by inflammation and vascular damage to non-lens tissues in the eye. Also, the radiation oxygen effect indicates different radiosensitivities for the vascular retina and the severely hypoxic lens. Therefore, this study uses the Monte Carlo N-Particle simulations to quantify dose conversion coefficients for several eye tissues for incident antero-posterior exposure to electrons, photons, and neutrons (and the tertiary electron component of neutron exposure). A stylized, multi-tissue eye model was developed by modifying a model by Behrens et al. (2009) to include the retina, uvea, sclera, and lens epithelial cell populations. Electron exposures were simulated as a single eye, whereas photon and neutron exposures were simulated employing two eyes embedded in the ADAM-EVA phantom. For electrons and photons, dose conversion coefficients are highest for either anterior tissues for low-energy incident particles or posterior tissues for high-energy incident particles. Neutron dose conversion coefficients generally increase with increasing incident energy for all tissues. The ratio of the absorbed dose delivered to each tissue to the absorbed dose delivered to the whole lens demonstrated the considerable deviation of non-lens tissue doses from lens doses, depending on particle type and its energy. These simulations demonstrate that there are large variations in the dose to various ocular tissues depending on the incident radiation dose coefficients; this large variation will potentially impact cataract development.

INTRODUCTION

There have been comprehensive animal and human reports on radiation-induced tissue damage for moderate or high doses (>0.5 Gy; low dose can be defined as ≤0.1 Gy, moderate dose >0.5 Gy and <1 Gy, and high dose ≥1 Gy). Brady and Yaeger (*1*) compiled the clinical injuries due to very high-dose exposures to eye tissues based on three reports by Merriam and colleagues in the late 1950s and early 1960s (*2, 3, 4*). It was noted whether exposures were single or fractionated and the general timeframe over which these injuries appear. For example, scarring of the cornea occurs one year after a fractionated absorbed dose of greater than 60 Gy delivered over a period of five to six weeks. Atrophy of the sclera occurs several years after a fractionated absorbed dose of 200–300 Gy (the timeframe over which this dose is delivered was not specified). Rubeosis (neovascularization) of the iris occurs several months to years after a fractionated absorbed dose of 70–80 Gy delivered over a period of six to eight weeks. Edema of the retina occurs several months after a fractionated absorbed dose of 20–35 Gy delivered over a period of two to four weeks. However, more recent assessments show low-dose extra-lenticular ocular diseases that are long-term health effects of atomic bomb survivors exposed to a mean dose of 0.5 Gy of mainly ionizing radiation of low linear energy transfer (LET). The ocular diseases include diabetic retinopathy, retinal arteriolosclerosis, retinal degeneration, and glaucoma, and are accompanied by systemic inflammation (*5, 6, 7*).

The classification of cataracts as either a tissue reaction with a threshold dose or a stochastic effect without a threshold is important. The present recommendation by the International Commission on Radiological Protection (ICRP) of a dose threshold of 0.5 Gy in effect indicates that the ICRP considers low and moderate doses to have negligible cataractogenic effect (*8*). Radio-induction of cataracts has historically been deemed a deterministic effect that has a dose threshold; for doses exceeding this threshold, cataractogenic severity increases and the latency decreases. Confirming the latency trend, Merriam et al. in 1972 (*9*) reported that the fractionated delivery of 2.50–6.50 Gy to radiotherapy patients from an external radiation beam resulted in the onset of cataract formation in this cohort occurring on average eight years and seven months after radiation exposure. Higher

[1] Address for correspondence: Chalk River Laboratories, Canadian Nuclear Laboratories, 286 Plant Road, Station 51A, Chalk River, ON, K0J 1J0, Canada; e-mail: richard.richardson@cnl.ca.

fractionated doses of 6.51–11.50 Gy resulted in the onset of cataract formation occurring on average four years and four months after radiation exposure.

In general, more recent studies generally report lower threshold doses than those studies reported decades earlier. A 2 Gy threshold was observed in radiation therapy patients by Merriam and Focht in 1957 (*3*), whereas a 0.08 Gy threshold was reported for Japanese atomic bomb survivors and Chernobyl cleanup workers by Shore et al. in 2010 (*10*). The ICRP defined in their 1990 recommendations (*8*) a threshold dose to the lens of 5 Gy for detectable lens opacities and 8 Gy for symptomatic cataracts. After ICRP 60 (*8*), the threshold dose for lens opacities and symptomatic cataracts was reduced 10-fold or more to 0.50 Gy in ICRP Publication 118 (*11*), and this threshold is applicable to single and fractionated exposures. Hamada et al. (*12*) indicated that establishment of this threshold by the ICRP was due in part to the findings presented by Nakashima et al. (*13*), Neriishi et al. (*14*), and Worgul et al. (*15*). However, evidence is mounting that the threshold, if it exists at all, is less than 0.10 Gy (*10, 14*).

To assess the risk of tissue damage or physiological changes due to radiation exposure that have the potential to promote cataractogenesis, the calculation of dose conversion coefficients for cataractogenic-sensitive tissues as a function of incident particle type and energy is required. Several studies have used Monte Carlo radiation transport codes to calculate dose conversion coefficients for the whole lens and parts of the lens. For example, Behrens et al. (*16*) developed a detailed model of the human eye (herein referred to as the BDZ eye model), and split the lens into the anterior third of the lens as the radiosensitive portion and the remaining posterior as the insensitive portion. They simulated irradiation by incident electrons to quantify the absorbed dose per unit of incident electron fluence delivered to the whole lens as a function of incident electron energy. This model was upgraded in 2011 by simulating the irradiation of two BDZ eyes embedded inside the ADAM-EVA phantom of the adult body. This merged simulation will be referred to as the BDZ eye-body model. Data were provided for incident photons to the lens components as a function of incident photon energy (*17*).

Manger et al. (*18*) also simulated the irradiation of two BDZ eyes within the adult UF-ORNL phantom (*19*). They quantified the absorbed dose per unit incident neutron fluence delivered to the radiosensitive portion and the whole lens as a function of incident neutron energy. Finally, Nogueira et al. (*20*) developed a detailed eye model based on anthropometric and composition data obtained from the National Council on Radiation Protection and Measurements (NCRP) report 130 (*21*) and data from Worgul (*22*). The germinative zone is considered the most radiosensitive component of the eye, as induction of posterior subcapsular and cortical cataracts involves aberrant differentiation of the lens epithelial cells (LECs) of high mitotic activity (*23, 24*). In the eye model by Nogueira et al. (*20*), the four zones of the LECs were implemented, including the germinative zone. A single, bare-eye model was exposed to an electron field, and the absorbed dose per unit incident electron fluence was quantified.

The etiology of each of the primary age-related cataracts [nuclear cataracts, cortical cataracts, and posterior subcapsular cataracts (PSCs)] is different and multifactorial. It involves different degrees of aging, heritability, and oxidative-stress-promoting factors, such as ionizing and non-ionizing radiations, diabetes, smoking, medications, myopia, and eye trauma (*25–27*). The most aging-related cataracts are the nuclear sclerotic cataracts that evolve slowly over time as the nucleus of the lens becomes yellow and cloudy, principally due to lens protein degradation. Nuclear cataracts may not be strongly induced by low doses, as ionizing radiation is significantly associated with systemic aging only at moderate or high doses (*28*). A characteristic of cortical cataracts is ion pump disruption and swelling of the cortex, resulting in spoke or wedge-like peripheral cloudiness; aberrant differentiation and migration of LECs are also involved (*24*). PSCs are formed by oxidation stress and ion pump disruption causing the aberrant differentiation and migration of LECs toward the posterior capsule of the lens. PSCs can occur in young individuals and risk factors for PSCs are ionizing radiation, steroid use, uveitis and diabetes (*27*). Jacob et al. (*29*) reviewed ionizing-radiation-induced cataracts in low- and moderate-dose epidemiological studies that included airline pilots, astronauts, atomic bomb survivors, and Chernobyl liquidators. All 15 studies demonstrated a general excess of cataracts with PSCs being the most prevalent radiation-induced cataract.

There is no definite evidence from radiation experiments for extra-lenticular irradiation of tissues being a cataractogenic factor; however, both radiation and non-radiation ocular research suggest otherwise. For example, oxidative stress as related to changes in radiation "oxygen effect" and to ocular oxygen gradients (see Discussion) are two etiological mechanisms that point to the involvement of extra-lenticular tissues in cataract development. Ocular oxygen gradients have a major effect on the type of cataract produced (*24*). The lens is the most hypoxic tissue in the body, with an oxygen partial pressure in the lens likely ranging from 1 to 2.5 mmHg or 0.33% O_2 (*30, 31*; references based on human and animal studies, respectively). Based on experimentation on the non-ocular oxygen effect, it can be inferred that the severely hypoxic LECs and lenses have a relatively low radiosensitivity compared to the well-oxygenated retina (~22 mmHg O_2) (*32*), which is known to be prone to ionizing radiation-induced damage (*33*). Another indication of extra-lenticular involvement in cataract development is that patients with retinitis pigmentosa have chronic ocular inflammation and aqueous flares, which have been identified as risk factors for PSC (*34*). The agents elevating PSC risk, such as steroids, diabetes, retinitis, and uveitis (inflammation of the choroid), all involve extra-lenticular damage to the eye (*27*).

The review of these studies indicates the need to quantify dose conversion coefficients as a function of incident particle type and energy, for LEC and fiber cell populations, for the whole lens, as well as for other eye tissues given their susceptibility to radiation damage. Therefore, this study developed a multi-tissue eye (MTE) model to obtain dose conversion coefficients for lens and non-lens tissues via Monte Carlo radiation transport simulations. The following section describes the methodology used to construct the MTE model and details the parameters employed in simulations using the Monte Carlo N-Particle 6 (MCNP6) version 2.0 radiation transport code. The following section first presents the dose conversion coefficients estimated for each eye tissue, and then the ratio of the absorbed dose delivered to each tissue to the absorbed dose delivered to the whole lens (referred to as the tissue:whole-lens dose ratio). The final section provides concluding remarks.

SIMULATION METHODOLOGY

Electron dose conversion coefficients were obtained from simulations involving the irradiation of a bare, single MTE model with a planar beam of electrons, whereas photon and neutron dose conversion coefficients were simulated by two MTE models embedded inside an ADAM-EVA phantom as described in appendix A of Behrens et al. (*17*) (known as the MTE-body model). All dose conversion coefficients were obtained for antero-posterior irradiation mode.

MTE and MTE-Body Model Development

The BDZ eye model (*16*) was extended to include the retina, uvea, sclera, and LEC populations in the lens; this new model is referred to as the MTE model. Figure 1 shows two-dimensional (2D) and three-dimensional (3D) views of the MTE model that incorporate the retina, uvea, sclera, and LEC populations within the lens. Table 1 lists the density, volume, mass, and isotopic composition of each component of the MTE model and of the phantom. The volume of each component of the MTE model was assessed by performing a MCNP 6.2 simulation that used stochastic ray tracing techniques (*35*) and the MCNP Visual Editor (*36*). A comparison of the dimensions and mass of the MTE model with prior published eye dosimetry models is given in the Discussion section.

The MTE-body model is shown in Fig. 2 as 3D views of the pair of modified stylized eyes embedded in an ADAM-EVA phantom that is composed of four elements (*37*), Table 1. The phantom used in this study does not contain legs, as Behrens et al. (*17*) demonstrated that for incident photons, the contribution of the trunk of the phantom to dose delivery to the lens is less than 1%. Supplementary Fig. S1 and information (https://doi.org/10.1667/RADE-23-00023.1.S1) describes in detail how the MTE model was developed, and provides a detailed schematic incorporating the sclera, cornea, uvea, retina, and LEC populations.

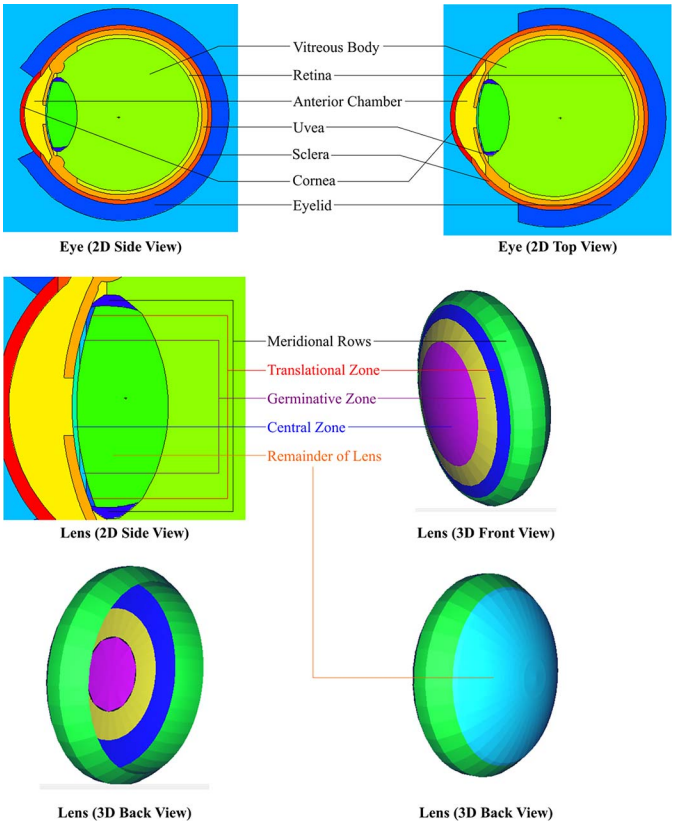

FIG. 1. Views of MTE model generated from MCNP Visual Editor (*36*).

Simulation Settings and Conversion of Tally Results to Dose Conversion Coefficients

In the MCNP 6.2 simulations, default physics models were employed with transport lower cutoff energies of 10^{-3} MeV, 10^{-3} MeV, and 0.00 MeV for electrons, photons, and neutrons, respectively (*35*). A total of 10^{10} source particles were used. For all simulation sets, electron transport cross-sections were obtained from the el03 library, whereas photon transport cross-sections were obtained from the mcplib84 library (*38*). For incident neutron simulations, transport cross-sections were obtained from the endf71x library. All simulations were carried out on a high-performance computing cluster at Canadian Nuclear Laboratories (CNL).

For incident electron simulations, secondary photon transport was enabled, and the total electron kinetic energy deposited in each component per source electron was determined for each eye component. The planar electron beam had a cross-section of 6 cm × 6 cm to encompass the cross-section of the eye.

For incident photon simulations, secondary electron transport was enabled in all eye components, and in the upper and middle part of the head. The total electron kinetic energy deposited in each component per source photon was determined for each eye component in the left and right eyes. The planar photon beam has a cross-section of 40 cm × 93 cm, and irradiated the entire head and trunk of the ADAM-EVA

TABLE 1
Properties of Eye Tissues in MTE Model

Tissue	Isotopic composition (% mass fraction)									Density (g cm^{-3})	Volume (cm^3)	Mass (g)
	H	C	N	O	Na	P	S	Cl	K			
Meridional rows[a]										1.06	2.11×10^{-2}	2.24×10^{-2}
Translational zone[a]										1.06	4.66×10^{-3}	4.94×10^{-3}
Germinative zone[a]	9.60	19.50	5.70	64.60	0.10	0.10	0.30	0.10	-	1.06	4.19×10^{-3}	4.44×10^{-3}
Central zone[a]										1.06	3.66×10^{-3}	3.88×10^{-3}
Remainder of lens[a]										1.06	1.83×10^{-1}	1.93×10^{-1}
Vitreous body[a]	11.20	-	-	88.80	-	-	-	-	-	1.0089	4.34	4.38
Retina[b]	10.00	14.60	4.50	70.60	-	-	0.30	-	-	1.07	5.40×10^{-1}	5.78×10^{-1}
Anterior chamber[a]	11.20	-	-	88.80	-	-	-	-	-	1.003	2.30×10^{-1}	2.30×10^{-1}
Uvea[b]	10.00	14.60	4.50	70.60	-	-	0.30	-	-	1.07	1.19	1.27
Sclera[b]	10.00	14.60	4.50	70.60	-	-	0.30	-	-	1.07	9.12×10^{-1}	9.76×10^{-1}
Cornea[a]	10.16	12.62	3.69	73.14	0.0065	0.0065	0.195	0.065	-	1.076	6.66×10^{-2}	7.17×10^{-2}
Eyelid[a]	10.00	20.40	4.20	64.50	0.20	0.10	0.20	0.30	0.10	1.09	4.39	4.78
Top of phantom head[c]										1.11[d]	1.10×10^3	1.22×10^3
Middle of phantom head[c]										1.11[d]	2.97×10^3	3.30×10^3
Bottom of phantom head[c]										1.11[d]	8.07×10^2	8.96×10^2
Trunk of phantom[c]	10.12	11.10	2.60	76.18	-	-	-	-	-	1.11[d]	3.97×10^4	4.41×10^4

[a] Isotopic composition and density by Behrens et al. (16), including all components of the lens.
[b] Isotopic composition and density provided by Nogueira et al. (*20*).
[c] Behrens et al. (*17*) used the International Commission on Radiation Units and Measurements (ICRU) four-component soft tissue isotopic composition for all components of the phantom (tabulated in Reference *37*).
[d] Phantom density by Behrens et al. (*17*).

phantom (see Fig. 2), as in the Behrens et al. (*17*) study. In both the incident electron and incident photon simulations, the "nearest group boundary" treatment was chosen for electron transport (*35*).

For incident neutron simulations, secondary photon [emitted from (n,γ) capture reactions] and tertiary electron (liberated from scatter interactions undergone by secondary photons) transports were enabled throughout the MTE-body model for a. neutron transport to determine the collision heating in each component per source neutron, b. secondary photon transport to determine the collision heating in each component per source neutron, and c. tertiary electron transport. In these three cases a–c, the total kinetic energy deposited in each component per source neutron was determined for both the left and right eye components. The planar neutron beam has a cross-section of 16 × 25 cm, and irradiates the entire head of the ADAM-EVA phantom as in the Manger et al. (*18*) study (see Fig. 2).

To convert the tally value of the energy deposited in each eye component into an absorbed dose (or kerma, which

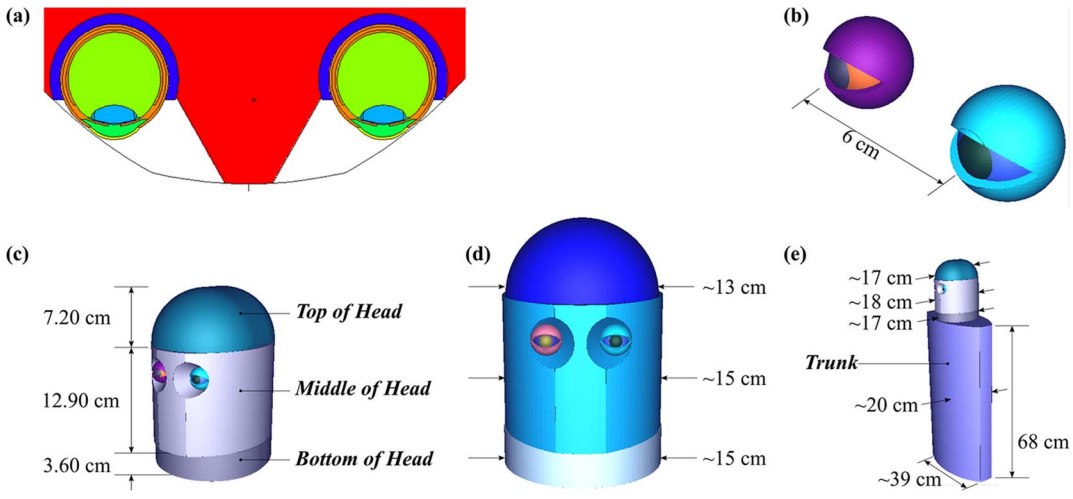

FIG. 2. Views of MTE models embedded in ADAM-EVA phantom generated from MCNP Visual Editor (*36*). Panel (a): 2D view of multi-tissue eyes coloured by material composition (eye on the right in image is designated as the left eye). Panel (b): 3D view of multi-tissue eyes centered 6 cm apart. Panel (c): 3D view of the three components of phantom head. Panel (d): Head-on 3D view of phantom head. Panel (e): 3D view of overall ADAM-EVA phantom including trunk.

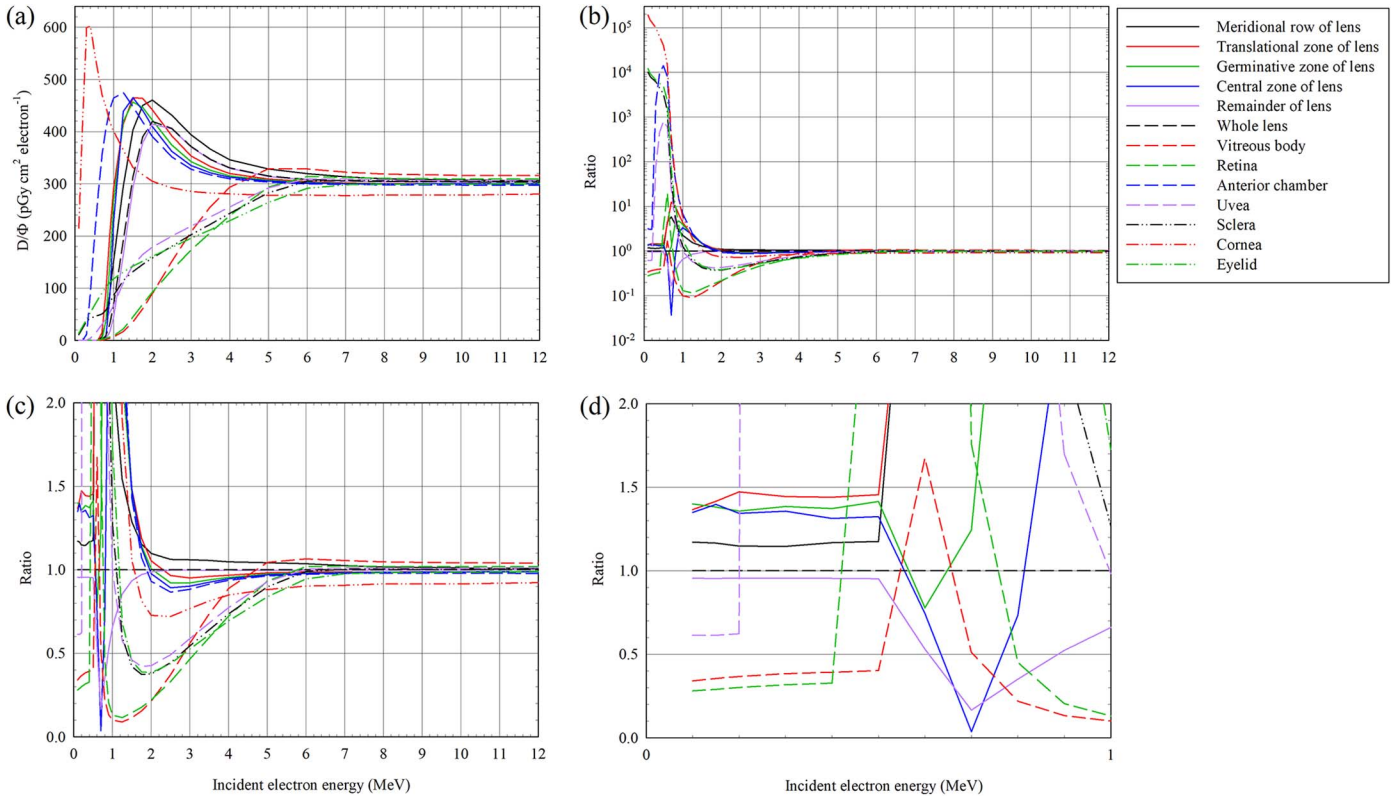

FIG. 3. Panel (a): Absorbed dose per unit incident electron fluence for eye tissues in MTE model. Panel (b): Tissue:whole-lens dose ratio. Panel (c): Tissue:whole-lens dose ratio (same as panel b, but zoomed vertical scale). Panel (d): Tissue:whole-lens dose ratio (same as panel b, but zoomed vertical and horizontal scale).

means "kinetic energy released per unit mass") per unit incident particle fluence, the following equation was used:

$$\frac{\left(\frac{1}{n}\sum_{i=1}^{n} T_i \ \frac{\text{MeV}}{\text{g} \times \text{source particle}}\right)\left(1.602 \times 10^{-13} \ \frac{\text{J}}{\text{MeV}}\right) \times \left(1 \ \frac{\text{Gy}}{\text{J/kg}}\right)\left(10^{-12} \ \frac{\text{Gy}}{\text{pGy}}\right)^{-1}\left(10^{3} \ \frac{\text{g}}{\text{kg}}\right)}{\frac{1}{A} \ \frac{\text{source particle}}{\text{cm}^2 \times \text{source particle}}}$$

Parameter A denotes the area of the planar source used in the simulation (in cm^2), and the resultant absorbed dose per incident particle fluence has a unit of pGy cm^2 source particle^{-1}. For incident electron simulations, $n = 1$ and T_1 (a single eye) is equal to the MCNP *F8 kinetic energy deposition tally for an eye component divided by the component mass (in g). For incident photon simulations, $n = 2$ and T_1 and T_2 denote the MCNP *F8 kinetic energy deposition tally for an eye component divided by the mass of the left eye and right eye components, respectively, or incident neutrons (case a), to obtain the neutron kerma per incident neutron fluence, denoted by $(K/\Phi)_n$, $n = 2$ and T_1 and T_2 denote the MCNP F6 kerma tally for the two eyes. Similarly for case b, the secondary photon kerma per incident neutron fluence, denoted by $(K/\Phi)_\gamma$, $n = 2$ and T_1 and T_2 are the MCNP F16 kerma tally for both eye components. For case c, the tertiary electron absorbed dose per incident neutron fluence is denoted by $(D/\Phi)_e$, and $n = 2$ and T_1 and T_2 are the MCNP *F8 kinetic energy deposition tally for both eye components.

RESULTS

Incident Electrons – Absorbed Dose

The absorbed doses per unit incident electron fluence as a function of incident electron energy for each eye tissue are illustrated in Fig. 3a and listed in Supplementary Table S1 (https://doi.org/10.1667/RADE-23-00023.1.S2). Due to the low range of electrons with energy below 0.50 MeV, the doses to LEC populations and to the remainder of the lens are low, as noted by Behrens et al. (*16*). The cornea, LEC populations, and remainder of the lens are in the anterior of the eye, and consequently possess a peak electron dose between 1 and 2 MeV. However, for deeper-lying tissues, namely the vitreous body, retina, uvea, sclera, and eyelid (the eyelid is schematically, not realistically, modeled (*16*) as encompassing the eyeball, apart from the cornea), generally doses increase with increasing incident electron energy and range. This is because electrons enter the eye and while traversing these tissues, achieve their Bragg peak just before these particles come to rest.

To show how the non-lens tissue doses deviated from the whole-lens doses, Fig. 3b plots the tissue:whole-lens dose

ratio and Fig 3c provides a zoomed vertical axis. The tissue:whole-lens dose ratio is highest, on the order of 10^3–10^5, for low incident electron energies for anterior tissues and for tissues that have extents in the anterior portion of the eye, namely the cornea, anterior chamber, sclera, and eyelid (Fig. 3b). The tissue:whole-lens dose ratio is in the vicinity of unity for LEC populations exposed to low-energy electrons (Figs. 3c and 3d). This ratio is around unity for all tissues for electron energies >4 MeV, indicating uniform dose delivery throughout the entire eye for this incident electron energy range.

Incident Photons – Absorbed Dose

The dose conversion coefficient as a function of incident photon energy for all tissues is illustrated in Fig. 4a and listed in Supplementary Table S2 (https://doi.org/10.1667/RADE-23-00023.1.S2). Figure 4a exhibits two peaks with a valley separating the peaks for all ocular tissues, a trend shown by Behrens et al. (*17*). The first peak, centered at $\sim 10^{-2}$ MeV, generally follows the curvature of the photon energy-dependent Compton scatter cross-section for hydrogen, carbon, nitrogen, and oxygen, whose peak values are at 1.50×10^{-2} MeV, 3×10^{-2} MeV, 4×10^{-2} MeV, and 4×10^{-2} MeV, respectively (*39*). The second peak, at high incident energies of 0.70–7 MeV, is believed to be due to the higher kinetic energy of secondary electrons liberated by incident photons in this energy range (relative to incident photons that produced the first peak). Assuming that the buildup of incident photons occurs at shallow depths into the eye, the liberated and high energy secondary electrons will traverse the anterior lying tissues with relatively low stopping power, resulting in low dose delivered to these tissues. As these electrons reach the posterior lying tissues, they may achieve their Bragg peak, resulting in a significant absorbed dose delivered. This results in the second peak being more pronounced for posterior lying tissues.

For incident photon energies below 10^{-2} MeV, the tissue:whole-lens ratio for anterior-lying tissues, namely the anterior chamber and cornea, are orders of magnitude above unity (Fig. 4b; Fig. 4c provides a zoom-in view of Fig. 4b as the vertical scale of the tissue:whole-lens dose ratio in Fig. 4c is confined to 0 to 2, providing a clearer view of the ratio's variation as a function of incident photon energy for all tissues). This is due to the buildup of low-energy incident photons in these anterior tissues, which then receive a higher absorbed dose relative to the relatively deeper-lying whole lens. Between incident photon energies of about 10^{-2} MeV and 0.70 MeV, the tissue:whole-lens ratio is close to unity for each tissue, suggesting uniform dose delivery throughout the eye. For incident photon energies above 0.70 MeV, the ratios depart from unity. For anterior tissues, the tissue:whole-lens ratios are less than unity, whereas for posterior tissues, the ratios are above unity as these >0.70 MeV photons are able to travel deeper into the eye and deposit less dose to anterior tissues and greater dose to deeper-lying tissues.

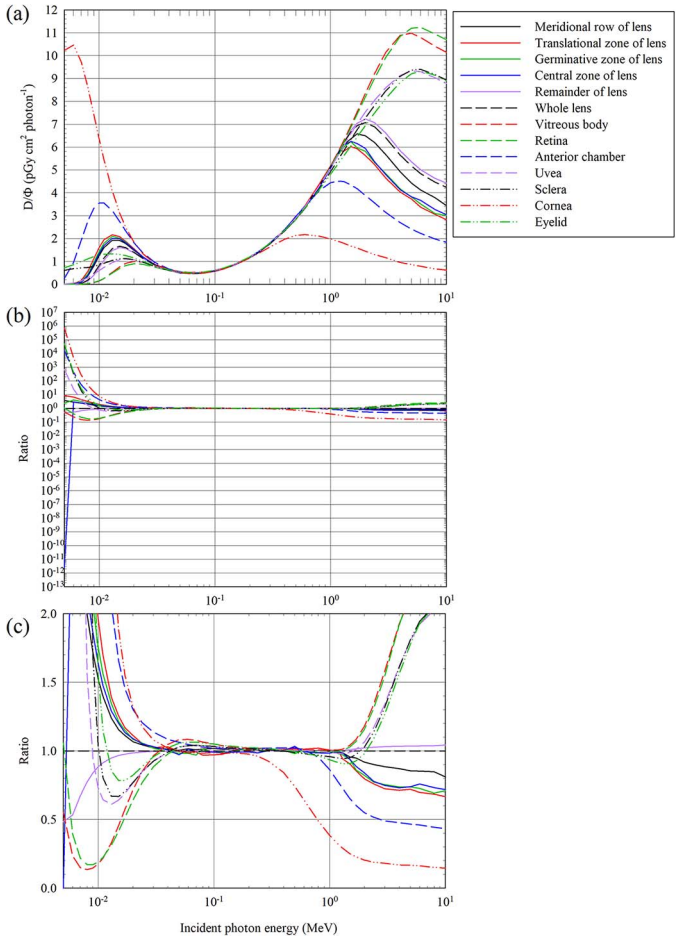

FIG. 4. Panel (a): Absorbed dose per unit incident photon fluence for eye tissues in MTE-body model. Panel (b): Tissue:whole-lens dose ratio. Panel (c): Same tissue:whole-lens dose ratio but with a zoomed vertical scale.

Incident Neutrons

The dose conversion coefficients for the total dose versus neutron energy are evaluated in terms of both the kerma and the absorbed dose; the former is due to kerma from neutrons and the latter is due to the absorbed dose from tertiary electrons. Presented below is a description of various parameters for each tissue and as a function of incident neutron energy: the neutron kerma, the tertiary electron absorbed dose, the total dose (neutron kerma plus tertiary electron absorbed dose), the percent contribution of the tertiary electron absorbed dose to the total dose, and finally the tissue:whole-lens total dose ratio. In the following discussion of the trends found in these quantities, the following nuclear reactions are referred to: $^{1}H(n,\gamma)^{2}H$ ($Q = +2.20$ MeV), $^{12}C(n,\gamma)^{13}C$ ($Q = +4.95$ MeV), and $^{14}N(n,p)^{14}C$ ($Q = +0.626$ MeV) (a positive Q value represents the energy released from a nuclear reaction not including the initiating neutron energy (*40*)). In addition, the following terminology is used to categorize neutron energies: neutrons with energy less than 10^{-6} MeV are referred to as "slow neutrons," neutrons with energy between 10^{-6} and 10^{-3}

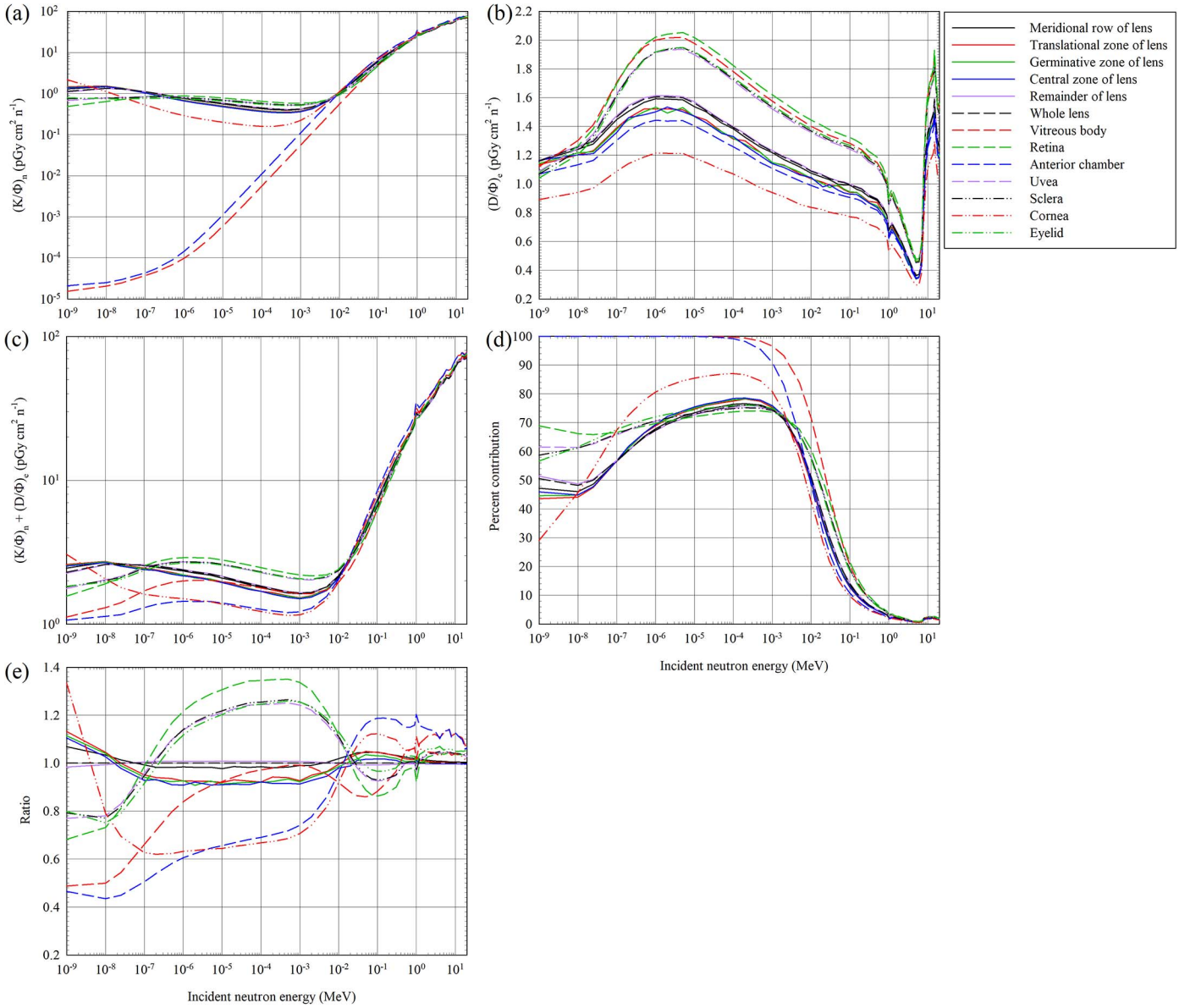

FIG. 5. Trends for all eye tissues in the MTE-body model. Panel (a): Neutron kerma per unit incident neutron fluence (numerical values in Supplementary Table S3; https://doi.org/10.1667/RADE-23-00023.1.S2). Panel (b): Tertiary electron absorbed dose per unit incident neutron fluence (Supplementary Table S4; https://doi.org/10.1667/RADE-23-00023.1.S2). Panel (c): Neutron kerma plus tertiary electron absorbed dose per unit incident neutron fluence (Supplementary Table S5; https://doi.org/10.1667/RADE-23-00023.1.S2). Panel (d): Percent contribution of tertiary electron absorbed dose to sum of neutron kerma plus tertiary electron absorbed dose. Panel (e): Tissue:whole-lens ratio for sum of neutron kerma plus tertiary electron absorbed dose.

MeV are referred to as "intermediate neutrons," and neutrons with energy above 10^{-3} MeV are "fast neutrons."

Neutron Kerma

For all tissues except the anterior chamber and vitreous body, there is a subtle decrease in the kerma with increasing incident neutron energies between 10^{-7} (thermal neutrons) and 10^{-3} MeV (resonance neutrons), as illustrated in Fig. 5a and listed in Supplementary Table S3 (https://doi.org/10.1667/RADE-23-00023.1.S2). This may be attributed to the decrease in the microscopic cross-section for the $^{14}N(n,p)^{14}C$ reaction, which is the primary contributor to kerma in this energy range. The magnitude of this decrease is most pronounced for the cornea, the most anterior tissue, and less pronounced for posterior ocular tissues, as incident neutrons may become thermalized prior to reaching these deeper-lying tissues. This results in more $^{14}N(n,p)^{14}C$ reactions occurring in these tissues relative to the cornea.

For incident neutron energies below 10^{-3} MeV (thermal and resonance neutrons), the kerma for the anterior chamber and vitreous body are orders of magnitude lower than those of other tissues; this is due to the absence of nitrogen in these two tissues (Table 1). As a result, neutrons traversing these two

tissues impart kerma via elastic scatter interactions; however, due to the low energy of these incident neutrons, the kinetic energy imparted to recoil nuclei are orders of magnitude lower than the 0.626 MeV Q value of the $^{14}N(n,p)^{14}C$ reaction that occurs in other tissues for this incident energy range. Above 10^{-3} MeV incident neutron energy (fast neutrons), elastic scatter collisions are the primary contributor to kerma for all tissues. As the incident neutron energy increases, so too does the kinetic energy imparted to recoil nuclei and, therefore, the neutron kerma.

The use of kerma to approximate absorbed dose warrants examination. The kerma approximation was used in the MCNP6 simulations for two reasons. The first reason is that it does not require the transport of secondary charged particles, resulting in shorter simulation run times. The second is that the MCNP6 code is not able to model the transport of the secondary proton and residual ^{14}C nucleus emitted from the $^{14}N(n,p)^{14}C$ reaction (*35*), and therefore the kinetic energy deposited in any tissue from this reaction would not be accounted for in the absorbed dose calculation if the approach using secondary charged particle transport were pursued. With respect to the adequacy of using the kerma approximation, it is assumed that if the thickness or depth of a tissue is greater than the range of the lightest, most energetic secondary charged particle that a neutron liberates, then kerma and absorbed dose are equivalent in this scenario. For neutron irradiation of the eye, recoil ^{1}H nuclei are the lightest secondary charged particles that can be liberated. The thinnest, most anterior-lying tissue in the eye model shown in Fig. 1 is the cornea, and the schematic in Supplementary Fig. SA1 (https://doi.org/10.1667/RADE-23-00023.1.S1) indicates that the thickness of the cornea is 5.89×10^{-2} cm. A 6.50 MeV recoil ^{1}H nucleus has a range approximately equal to this thickness. This is the range in skeletal muscle, which has a density of 1.04 g cm^{-3} and the following isotopic composition (similar to that of eye tissues) in percent mass fraction: 10.06%, 10.78%, 2.77%, and 75.48% for ^{1}H, ^{12}C, ^{14}N, and ^{16}O, respectively (*41*). Therefore, for incident neutron energies below 6.50 MeV, kerma and absorbed dose are equivalent. For incident neutron energies above 6.50 MeV, there are select anterior tissues listed in Table 2 whose thickness or depth (evaluated along the x axis in reference to Supplementary Fig. S1; https://doi.org/10.1667/RADE-23-00023.1.S1) are less than the corresponding range of the highest energy recoil ^{1}H nuclei that can be liberated, and for these tissues kerma exceeds absorbed dose. Therefore, the neutron kerma delivered to these tissues for incident neutron energies above 6.50 MeV are conservative relative to the absorbed dose delivered.

TABLE 2
Identification of Tissues for which Kerma Exceeds Absorbed Dose

Incident neutron energy (MeV)	Range of most energetic recoil ^{1}H nucleus in skeletal muscle (cm) (*41*)	Tissue	Thickness or depth into eye (cm)[a]
7	6.36×10^{-2}	Cornea	5.89×10^{-2}
8	8.05×10^{-2}		
9	0.10		
10	0.12		
12	0.16		
14	0.22		
15	0.25		
16	0.27		
18	0.35	Cornea	5.89×10^{-2}
		Vitreous body	0.34
		Iris	0.34
20	0.41	Cornea	5.89×10^{-2}
		Vitreous body	0.34
		Iris	0.34
		Central zone of lens	0.37
		Germinative zone of lens	0.40

[a] In reference to Fig. SA1, depth is defined as the difference between the x position of the posterior-most surface of a tissue and that of the anterior surface of the cornea.

Tertiary Electron Absorbed Dose

The tertiary electron absorbed dose per unit incident neutron fluence as a function of incident neutron energy exhibits two peaks, one centered at approximately 5×10^{-6} MeV and the other centered at 15 MeV, as illustrated in Fig. 5b and listed in Supplementary Table S4 (https://doi.org/10.1667/RADE-23-00023.1.S2). The first peak is due to the $^{1}H(n,\gamma)^{2}H$ reaction. The cross-section for this reaction is 1.67 barn at 10^{-9} MeV, 0.024 barn at 5×10^{-6} MeV, and 3.39×10^{-5} barn at 1 MeV (*42*). Relative to 10^{-9} MeV thermal neutrons, 5×10^{-6} MeV resonance neutrons are able to penetrate deeper into the eye prior to possibly thermalizing and undergoing the $^{1}H(n,\gamma)^{2}H$ reaction. Therefore, the spatial points of emission for the secondary 2.20 MeV gamma rays and subsequent tertiary electrons are located deeper into the eye. These electrons may have to travel a finite distance to arrive at a tissue, and in so doing, will experience an increase in stopping power, thereby enabling delivery of a higher absorbed dose. This is a proposed reason for the presence of the first peak.

For any tissue, the decrease in the absorbed dose when the incident neutron energy increases from 5×10^{-6} MeV resonance neutrons to 1 MeV fast neutrons is attributed to the $^{1}H(n,\gamma)^{2}H$ reaction cross-section decreasing by one order of magnitude. This lower cross-section at 1 MeV is not totally offset by the proposed reason for the presence of the first peak, which is the increase in the depth into the eye that incident neutrons are absorbed and the subsequent increase in the stopping power of the tertiary electrons generated. Fig. 5b indicates that the lowest-magnitude curve is for the most anterior-lying tissue (cornea) and greatest for the deepest-lying tissues such as the retina. This is due to the buildup of thermalized and absorbed neutrons at some finite depth into the eye, resulting in more

tertiary electron absorbed dose in deeper-lying tissues than in anterior-lying tissues.

The second peak is due to the $^{12}C(n,\gamma)^{13}C$ reaction; the peak spans from 5–20 MeV and is centered at 15 MeV. The shape of this peak partially follows that of the microscopic cross-section for this reaction as a function of energy, in that the cross-section is 6.29×10^{-5} barn at 5 MeV, 1.61×10^{-4} barn at 15 MeV, and 2.11×10^{-4} barn at 20 MeV (*42*). The ratio of the tertiary electron absorbed dose to the photon kerma for each tissue and as a function of incident neutron energy is shown in Supplementary Fig. S2 (https://doi.org/10.1667/RADE-23-00023.1.S3). For most ocular tissues, this ratio is between 0.85 and 1.00 for the full range of neutron energies, except for the most anterior tissues.

Total Dose (Neutron Kerma Plus Tertiary Electron Absorbed Dose), Tissue:Whole-Lens Ratio

For most tissues, the total dose delivery for incident neutron energies below 10^{-3} MeV, as illustrated in Fig. 5c and listed in Supplementary Table S5 (https://doi.org/10.1667/RADE-23-00023.1.S2), is dominated by the tertiary electrons. This is illustrated in Fig. 5d, in which the percent contribution to the total dose from tertiary electrons for neutrons below 10^{-3} MeV is greater than 50% for most tissues. Therefore, the peak structure for neutron energies below 10^{-3} MeV of the total dose shown in Fig. 5c follows a similar trend to that of the tertiary electron absorbed dose shown in Fig. 5b. For incident neutron energies above 10^{-3} MeV, the neutron kerma increasingly exceeds tertiary electron absorbed dose (Fig. 5a and c). An observation concerning Fig. 5c is that unlike in Fig. 5a, the curves pertaining to the anterior chamber and vitreous body are now of the same order of magnitude as the curves for other tissues for incident neutron energies below 10^{-3} MeV. Due to the absence of nitrogen in the anterior chamber and vitreous body, tertiary electron absorbed dose delivered to these two tissues is far greater than neutron kerma for this incident neutron energy range.

The tissue: whole-lens dose ratio varies between 0.80 and 1.20 for incident neutrons with energy above 10^{-3} MeV (Fig. 5e). Below this energy, the tissue:whole-lens dose ratio varies more significantly (between 0.50 and 1.30) due to the changing contribution of the $^{1}H(n,\gamma)^{2}H$ reaction to the overall dose for each tissue in this low-energy range.

DISCUSSION AND CONCLUSION

The Need for an MTE Model

This work has estimated radiation dose to specific tissues in the eye that likely contribute to the development of cataracts. There is evidence from reported non-radiation studies that cataractogenesis is multifactorial, and that it especially involves abnormal oxygen levels and occurs at multiple sites, particularly as aging and inflammation are often etiological cataractogenic factors. There is also evidence that the etiology of different primary types of cataracts involves different ocular sites. Consequently, the development of multi-site criteria for the development of radiation-induced cataracts would give better estimates of vulnerability to premature cataractogenesis.

An examination of a limited number of pathological changes associated with the common primary types of cataracts indicated that different cataract types have different radiation target tissues in the eye (*24*). Cortical cataracts and PSCs appear to have more mutual pathological characteristics than nuclear cataracts have with them. Cortical cataracts and PSCs primarily present with abnormal differentiation of LECs that have a normal complement of organelles, whereas nuclear cataracts chiefly involve the unfolded protein response in the organelle-free zone of the central portion of the lens. The respective risks from exposure to electrons, photons, and neutrons can be assessed for cortical cataracts and PSCs by using data presented here for the LEC germinative zone; however, the whole lens would be a substitute target for the organelle-free zone for nuclear cataracts.

Although the whole lens is the traditional cataractogenic target, there are several considerations that point to nuclear cataracts being rarely induced by low-dose radiation. The radiation oxygen effect is particularly relevant in demonstrating that the lens has protection from radiation-induced cataractogenesis due to the lens being the most hypoxic tissue in the body. The trend in the oxygen enhancement ratio of radiation-induced cell death and other endpoints can be explained by radiation-induced reactive oxygen species reacting with DNA or alternatively by the induction of reactive oxygen species generated by mitochondria (*43*). Based on data obtained from animal studies, over 90% of mammalian oxygen consumption is by mitochondria, which are also the major cellular source of reactive oxygen species (*44*). However, the lens has a very low mitochondrial content, thereby minimizing radiation-induced reactive oxygen species and aging-related oxidation stress of everyday life to the non-dividing fiber cells of adults (*24*). The fiber cells of the central lens, the nucleus, are a completely organelle-free zone. Consequently, the non-dividing fiber cells of the adult lens nucleus normally reside in an ultra-low oxidative stress, minimally aging-related, and radioprotected environment.

The radiation oxygen effect is also relevant to non-lens tissues of the eye. Vascular regions especially, such as the retina and choroid layer of the uvea, have much higher oxygen and mitochondrial concentrations than the non-vascular lens, and consequently are particularly more prone to damage by normal oxidative stress and by ionizing radiation. In support of this viewpoint is that retinal DNA damage may be caused by mitochondrial oxidative stress in experimental autoimmune uveitis (*45*). Indeed, disrupted

mitochondrial function is a key phenomenon of astronauts subjected to microgravity and space radiation during spaceflights (*46*). Based on data obtained from animal studies, even low doses to mice of high-LET, high-charge, high-energy ions, such as galactic cosmic rays, affect the retinal vasculature, causing apoptosis of endothelial cells (*47*). Therefore, because of the oxygen effect and experimental evidence, it is important that dose coefficients for various radiation exposures to tissues such as the retina and uvea are evaluated.

Radiation exposure of the eye increases its oxidative stress, which is an important facet in development of all primary cataract types (*27*). This increase may be partially due to inducing oxygen level changes in the lens and non-lens tissues of the eye. Lens cells including LECs prefer a "Goldilocks" range of oxygen levels: too little or too much oxygen causes oxidative stress and cataracts (*24*). On the one hand, lower oxygen levels are possibly associated with PSCs and/or cortical cataracts (*48*). On the other hand, nuclear cataracts are promoted by higher-than-normal ocular oxygen levels, as experienced during hyperbaric therapy and likely by American astronauts using high-oxygen spacecraft atmospheres before 1976 (*49*). Ionizing radiation possibly alters vascular ocular sources of oxygen such as the iris and retina, and the passive transport of oxygen across the vitreous body (*27*), and hence the oxygen uptake by the avascular lens.

There are indications that ionizing radiation not only causes oxidative stress, but also alters oxygen levels. Systemic inflammation is closely associated with atomic bomb survivors (*50*) and a characteristic of chronic inflammation is that systemic tissues become profoundly hypoxic (*51*). Chronic ocular inflammation, including uveitis and retinitis, are significantly associated with radiotherapy (*33*) and independently with cataracts; PSCs especially are linked to chronic ocular inflammation (*24*). High-dose brachytherapy or external beam radiotherapy can increase retinal oxygenation and reduce blood flow in exposed eyes, consequently leading to radiation retinopathy (*33*). Astronauts enduring space radiation and microgravity have shown cerebro-ophthalmic effects including cataract and retinopathy, which are sometimes associated with specific neurocognitive deficits (*52*). Consequently, although the associations between low-dose radiation exposures, ocular oxygen alterations, and cataractogenesis have not been proven, there are grounds to consider this seriously in future research.

The MTE Model Compared to Other Published Dosimetry Eye Models

This study developed a new eye model, termed the MTE model, that contains a significant number of lens and non-lens tissues; however, the radiation doses are comparable to those of the ocular tissues that are found in the published models that our MTE model is based on. Our MTE model was developed based on the eye models presented in Behrens et al. (*16*) and Nogueira et al. (*20*), and on the data presented in NCRP report 130 (*21*). Overall, the dose conversion coefficients for the whole lens as a function of energy for incident electrons, photons, and neutrons match the qualitative trends described in Behrens et al. (*16*), Behrens et al. (*17*), and Manger et al. (*18*). Specifically, the resultant MTE model contains a germinative zone whose volume, mass, and thickness (defined as the difference in the x-bounds of the zone identified as surfaces 17 and 18 in Supplementary Fig. S1; https://doi.org/10.1667/RADE-23-00023.1.S1) are 4.19 mm^3, 4.44 mg and 0.275 mm respectively. The percentage difference between these quantities and those in the Nogueira et al. (*20*) eye model are 16%, 17% and 32%, respectively. Table 1 indicates that the mass of the overall lens in the MTE model is 224 mg, or $\sim$2% less than the 229 mg mass in the Behrens et al. (*16*) eye model. Therefore, for larger tissues such as the lens, the comparison of estimated dose coefficients shows very close agreement, with greater differences for smaller mass tissues such as the LEC populations.

This study demonstrated that for any incident radiation particle type and energy, there is spatial variation in the dose conversion coefficient delivered throughout the eye; quantifying this spatial variation was the key focus of this study. To validate the dose conversion coefficients obtained from the MTE model, the ratios were calculated with the MTE whole-lens dose coefficients as the numerator, and with the dose coefficients for incident electrons or photons published elsewhere (*16*) and (*17*), respectively, as the denominators (Fig. 6). The whole lens was chosen for this benchmarking for two reasons: this tissue is present in both the BDZ and MTE models, and the spatial position in the eye and the mass of this tissue in the two models are similar. The whole-lens coefficient and radiosensitive region of the lens coefficient are both plotted, and the latter only tabulated, for neutron exposures by Manger et al. (*18*). Their plot indicates no significant numerical difference between the two coefficients and it is therefore assumed that the coefficient for the whole lens is numerically equal to that for the radiosensitive region of the lens. Our Fig. 6 also plots the ratio of the whole-lens dose coefficient of the MTE model to that in the published in the literature (*18*) for neutron exposures.

Figure 6 indicates that for incident electrons and photons, the ratio is in the vicinity of unity except for low incident energies, <1 MeV for electrons and $<10^{-2}$ MeV for photons, where this ratio is above unity. A proposed reason for this is that in the BDZ model, incident particles need to traverse the cornea and anterior chamber to reach the whole lens. In the MTE model, incident particles need to traverse the cornea, sclera, anterior chamber, and uvea (iris) to reach the whole lens. The sclera and uvea contain carbon and nitrogen, and have a higher density than the anterior chamber (Table 1). For incident low-energy electrons, this results in these electrons losing more kinetic energy and

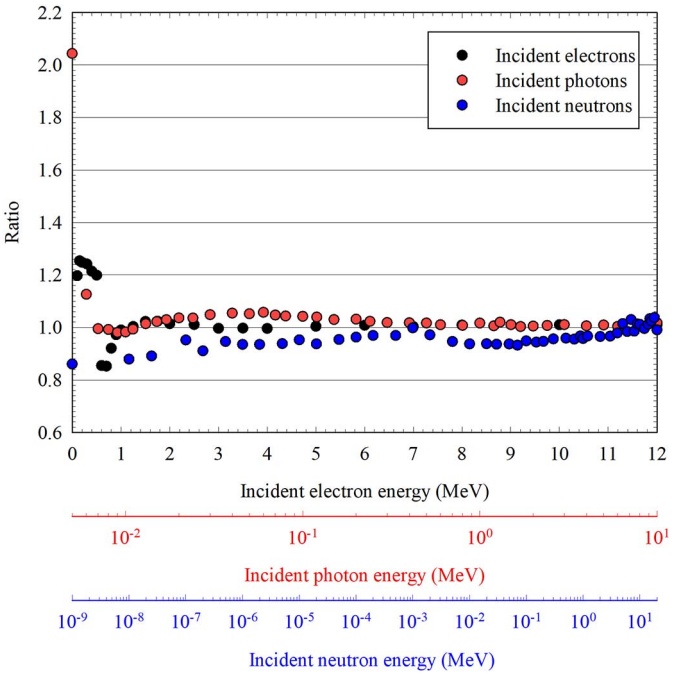

FIG. 6. Ratios of MTE whole-lens dose conversion coefficient to the coefficients published in references (*16*), (*17*) and (*18*) for incident electrons, photons and neutrons.

gaining higher stopping power prior to reaching the whole lens, thereby enabling electrons to deliver a higher absorbed dose to the whole lens in the MTE model relative to the BDZ model. For incident low-energy photons, there will be more buildup of these photons in the sclera and uvea, resulting in a higher absorbed dose delivered to the whole lens in the MTE model relative to the BDZ model.

For incident neutrons, the ratio is unity except for low incident energies (below 10^{-3} MeV) where the ratio is slightly below unity. One proposed reason for this is that the anterior chamber occupies the entire region between the cornea and whole lens in the BDZ model, whereas the sclera, anterior chamber, and uvea occupy this region in the MTE model. Given that the anterior chamber has a higher hydrogen mass concentration relative to the sclera and uvea, it follows that the mass of the anterior chamber and the mass of its hydrogen content are larger in the previously stated region for the BDZ model relative to the MTE model. Therefore, for low-energy incident neutrons in the BDZ model, there is more buildup in this region from the $^{1}H(n,\gamma)^{2}H$ capture reaction, and a greater absorbed dose is delivered to the whole lens relative to the MTE model. A limitation of the MTE model lies in the use of neutron collision heating kerma to compute the overall conversion coefficient for incident neutrons with energy above 6.50 MeV. It is therefore inevitable, as identified in Table 2, that the calculated coefficients for anterior-lying tissues overestimate those obtained based on secondary charged particle transport from neutron interactions.

Commentary on Eye Lens Dosimetry Measurement Techniques

There are several publications by the ICRP that tabulate dose conversion coefficients for a variety of external exposure scenarios and incident radiation types, among them are ICRP publications 74, 116 and 119 (*53, 54, 55*). These resources can be used to calculate the absolute dose delivered to target organs and tissues of interest for a known external field strength. For radiotherapy exposures, a variety of techniques exist to measure dose delivered among them are electronic portal imaging devices, gel dosimeters, and metal oxide semiconductor field effect transistor detectors (*56*). For whole-body exposures in occupational settings, thermoluminescent and optically stimulated luminescence technologies are typically used to measure dose from X ray, gamma ray, and beta exposures and CR-39 nuclear track detectors are used to measure dose from neutron exposures (*57*). With respect to the eye lens dosimetry measurements, Dubeau et al. (*58*) provides a detailed description of available eye lens dosimeters that seek to measure $H_p(3)$, personal dose equivalent delivered to a 3 mm depth in an ICRU cylindrical or slab phantom. $H_p(3)$ is an operational quantity that seeks to closely approximate the dose equivalent delivered to the eye lens (*59*). Commercially available eye lens dosimeters were deemed to provide a satisfactory response to photon radiation, while the response to beta radiation requires improvement (*60*). In addition, Dubeau et al. (*58*) found for neutron eye lens dosimetry, that a selection of commercially available passive neutron dosimeters exists, however their ability to accurately measure neutron eye lens dose has yet to be evaluated. Another study by Dubeau et al. (*61*) tested the response of five commercially available skin dosimeters each covered by a 300 mg cm^{-2} thick layer of polycarbonate. It was found that these dosimeters provide accurate readings of $H_p(3)$ for photon and beta radiation incident with a variety of angles and energy.

Hatami et al. (*62*) and Miyaji et al. (*63*) compared the eye lens and whole-body dose measured by several dosimetric technologies for medical-related radiation exposures. The former study was in relation to interventional cardiology and compared the doses to physicians delivered to thermoluminescent dosimeters (TLDs) positioned in the vicinity of the eyes and to TLDs placed in the vicinity of the chest. It was found that the whole-body dose was a few factors below that of the eye lens dose. The latter study positioned several dosimetry technologies in the vicinity of eyes, neck, chest, and abdomen of a RANDO human phantom. Here, a syringe filled with either ^{99m}Tc, ^{123}I, or ^{18}F was placed 30 cm from the abdomen of the phantom. It was found that for the previously mentioned radionuclides, the mean eye lens dose was within the uncertainty of the mean whole-body dose.

Future Work

A potential avenue for further research is to use the neutron-energy-dependent quality factor for hydrogen, carbon, oxygen, and nitrogen, tabulated by Siebert and

Schuhmacher (*64*), to quantify both the quality factor in each tissue due to neutron collisions with these four isotopes, and the quality factor in each tissue due to these neutron collisions and tertiary electron transport. Doing so will enable an understanding of how the quality factor changes throughout the eye for a fixed incident neutron energy, and an understanding of how the quality factor for each tissue changes with incident neutron energy. A second possible avenue for further research is to quantify, for a variety of angles of incidence, dose conversion coefficients for all tissues in the MTE model as a function of incident energy for electrons, photons, and neutrons. El Basha et al. (*65*) developed a scalable and deformable stylized eye model to account for changes in eye size and shape in adult populations. As the MTE model is defined inherently for a reference adult, an additional area of further development is to apply the scaling and deformation methodology presented elsewhere (*65*) to the MTE model to produce dose conversion coefficients suitable for patients with non-emmetropic eyes undergoing radiotherapy for ocular diseases.

Conclusion

A case has been made that cataractogenesis by low-dose radiation, unlike high-dose radiation, probably involves multiple tissues in the eye, targeting both lens and non-lens tissues. The different primary cataract types appear to justify different ocular tissue targets. Consequently, we have established an eye model that includes the LEC populations, and the vitreous, retina, uvea and sclera. The MTE model shows considerable variation in the doses to various ocular tissues, especially for low-energy incident particles. It is hypothesized that the dose conversion coefficients estimated will be modified by the oxygen effect due to oxidative stress and inflammation; therefore, experimental research is being pursued at CNL to quantify radiation-induced changes in oxygenation, inflammation, and oxidative stress biomarkers. Consequently the dose conversion coefficients generated for various ocular tissues can be modified to allow for the oxygen effect. There is a strong case that low dose and low-dose rates promote cataracts that have multifactorial etiology involving multiple ocular tissues. Therefore, it is of consequence for radiation protection assessments, that it has been demonstrated that there is a considerable difference between the absorbed doses delivered to various ocular tissues, compared to the dose delivered to the whole lens, which has traditionally been employed as a cataractogenic dosimetry target.

SUPPLEMENTARY INFORMATION

Supplementary Fig. S1 and supplementary information: MTE model development. https://doi.org/10.1667/RADE-23-00023.1.S1.

Supplementary Tables S1–S6: Tabulated dose conversion coefficients for MTE model. https://doi.org/10.1667/RADE-23-00023.1.S2.

Supplementary Fig. S2: Supplementary plot. https://doi.org/10.1667/RADE-23-00023.1.S3.

ACKNOWLEDGMENTS

This work was supported by Atomic Energy of Canada Limited's Federal Nuclear Science and Technology Work Plan. This research made use of the resources of the High Performance Computing Centre at CNL. The authors would like to thank Jovica Atanackovic at Ontario Power Generation for the assistance provided in developing the MTE model, Clifford Dugal at CNL for the assistance provided in running simulations at CNL's High Performance Computing Centre, and Marat Seydaliev at CNL for the helpful comments that guided the development of this paper.

Received: February 9, 2023; accepted: June 2, 2023; published online: July 7, 2023

REFERENCES

1. Brady LW, Yaeger TE. Radiation effects on the eye. In: Alberti WE, Richard G, Sagerman RHS, editors. Age-related macular degeneration. Berlin: Springer-Verlag; 2001.
2. Merriam Jr GR. Late effects of beta radiation on the eye. AMA Arch Ophthalmol 1955; 53(5):708–17.
3. Merriam Jr GR, Focht EF. A clinical study of radiation cataracts and the relationship to dose. Am J Roentgenol Radium Ther Nucl Med 1957; 77:759–85.
4. Merriam Jr GR, Biavati BJ, Bateman JL, Rossi HH, Bond VP, Goodman L, Focht EF. The dependence of RBE on the energy of fast neutrons: IV. Induction of lens opacities in mice. Radiat Res 1965; 25(1):123–38.
5. Hamada N, Azizova TV, Little MP. An update on effects of ionizing radiation exposure on the eye. Br J Radiol 2019; 20190829.
6. Hayashi T, Kusunoki Y, Hakoda M, Morishita Y, Kubo Y, Maki M, Kasagi F, Kodama K, Macphee DG, Kyoizumi S. Radiation dose-dependent increases in inflammatory response markers in A-bomb survivors. Int J Radiat Biol 2003; 79(2):129–36.
7. Neriishi K, Nakashima E, Akahoshi M, Hida A, Grant EJ, Masunari N, Funamoto S, Minamoto A, Fujiwara S, Shore RE. Radiation dose and cataract surgery incidence in atomic bomb survivors, 1986–2005. Radiol 2012; 265(1):167–74.
8. ICRP 60, 1990 Recommendations of the International Commission on Radiological Protection. Ann ICRP 1991; 21:1–201.
9. Merriam Jr GR, Szechter A, Focht EF. The effects of ionizing radiations on the eye. Front Radiation Ther Onc 1972; 6:346–85.
10. Shore RE, Neriishi K, Nakashima E. Epidemiological studies of cataract risk at low to moderate radiation doses: (not) seeing is believing. Radiat Res 2010; 174:889–94.
11. ICRP 118, Authors on behalf of I, Stewart FA, Akleyev AV, Hauer-Jensen M, Hendry JH, et al. ICRP publication 118: ICRP statement on tissue reactions and early and late effects of radiation in normal tissues and organs—threshold doses for tissue reactions in a radiation protection context. Ann ICRP 2012; 41:1–322.
12. Hamada N, Fujimichi Y, Iwasaki T, Fujii N, Furuhashi M, Kubo E, et al. Emerging issues in radiogenic cataracts and cardiovascular disease. J Radiat Res 2014; 55:831–46.
13. Nakashima E, Neriishi K, Minamoto A. A reanalysis of atomic-bomb cataract data, 2000–2002: a threshold analysis. Health Phys 2006; 90:154–60.
14. Neriishi K, Nakashima E, Minamoto A, Fujiwara S, Akahoshi M, Mishima HK, et al. Postoperative cataract cases among atomic bomb survivors: radiation dose response and threshold. Radiat Res 2007; 168:404–8.
15. Worgul BV, Kundiyev YI, Sergiyenko NM, Chumak VV, Vitte PM, Medvedovsky C, et al. Cataracts among Chernobyl clean-up workers: implications regarding permissible eye exposures. Radiat Res 2007; 167:233–43.

16. Behrens R, Dietze G, Zankl M. Dose conversion coefficients for electron exposure of the human eye lens. Phys Med Biol 2009; 54: 4069–87.
17. Behrens R, Dietze G. Dose conversion coefficients for photon exposure of the human eye lens. Phys Med Biol 2011; 56:415–37.
18. Manger RP, Bellamy MB, Eckerman KF. Dose conversion coefficients for neutron exposure to the lens of the human eye. Radiat Prot Dosim 2012; 148:507–13.
19. Lee C, Lodwick D, Hurtado J, Pafundi D, Williams JL, Bolch WE. The UF family of reference hybrid phantoms for computational radiation dosimetry. Phys Med Biol 2010; 55:339–63.
20. Nogueira, P, Zankl, M, Schlattl, H, Vaz, P. Dose conversion coefficients for monoenergetic electrons incident on a realistic human eye model with different lens cell populations. Phys Med Biol 2011; 56:6919–34.
21. Biological effects and exposure limits for hot particles. NCRP Report No. 130. Bethesda: National Council on Radiation Protection and Measurements; 1999.
22. Worgul BV. The Edward S Harkness Eye Institute resident's basic science study guide. New York: Columbia University Press; 1991.
23. Merriam Jr GR, Worgul BV. Experimental radiation cataract—its clinical relevance. Bull N Y Acad Med 1983; 59:372–92.
24. Richardson RB. The role of oxygen and the Goldilocks range in the development of cataracts induced by space radiation in US astronauts. Exp Eye Res 2022:109192.
25. West S. Epidemiology of cataract: accomplishments over 25 years and future directions. Ophthalmic Epidemiol 2007; 14:173–8.
26. Chang JR, Koo E, Agrón E, Hallak J, Clemons T, Azar D, et al. Risk factors associated with incident cataracts and cataract surgery in the Age-related Eye Disease Study (AREDS): AREDS report number 32. Ophthalmol 2011; 118:2113–9.
27. Richardson RB, Ainsbury EA, Prescott CR, Lovicu FJ. Etiology of posterior subcapsular cataracts based on a review of risk factors including aging, diabetes, and ionizing radiation. Int J Radiat Biol 2020; 96:1339–61.
28. Richardson RB. Ionizing radiation and aging: rejuvenating an old idea. Aging (Albany NY) 2009;1(11):887–902.
29. Jacob S, Michel M, Brézin AP, Laurier D, Bernier MO. Ionizing radiation as a risk factor for cataract: what about low-dose effects? J Clin Exp Ophthalmol. 2012; S1-005:1–7
30. Helbig H, Hinz JP, Kellner U, Foerster MH. Oxygen in the anterior chamber of the human eye. Ger J Ophthalmol. 1993; 2(3):161–4.
31. Giblin FJ, Quiram PA, Leverenz VR, Baker RM, Dang L, Trese MT. Enzyme-induced posterior vitreous detachment in the rat produces increased lens nuclear pO_2 levels. Exp Eye Res 2009; 88 (2):286–92.
32. Beebe DC, Shui YB, Siegfried CJ, Holekamp NM, Bai F. Preserve the (intraocular) environment: the importance of maintaining normal oxygen gradients in the eye. Jpn J Ophthalmol 2014; 58(3):225–31.
33. Rose K, Krema H, Durairaj P, Dangboon W, Chavez Y, Kulasekara SI, et al. Retinal perfusion changes in radiation retinopathy. Acta Ophthalmol. 2018; 96(6):e727–e731.
34. Fujiwara K, Ikeda Y, Murakami Y, Funatsu J, Nakatake S, Tachibana T, et al. Risk factors for posterior subcapsular cataract in retinitis pigmentosa. Invest Ophthalmol Vis Sci 2017; 58:2534–7.
35. MCNP® User's Manual Code Version 6.2. Manual Rev. 0. Los Alamos: Los Alamos National Laboratory; 2017.
36. MCNP/MCNPX Visual Editor Computer Code Manual. Schwarz Software & Consulting, LLC; 2011.
37. Compendium of Material Composition Data for Radiation Transport Modeling Revision 1. PIET-43741-TM-963, PNNL-15870 Rev. 1. Richland: Pacific Northwest National Laboratory; 2011.
38. Listing of Available ACE Data Tables. LANL Report LA-UR-13-21822. Los Alamos: Los Alamos National Laboratory; 2014. (https://www.osti.gov/biblio/1068959)
39. National Institute of Standards and Technology. (2010). XCOM: Photon Cross Sections Database. Retrieved May 2022 from https://physics.nist.gov/PhysRefData/Xcom/html/xcom1.html
40. National Nuclear Data Center. Q-value Calculator (QCalc). Retrieved May 2022 from https://www.nndc.bnl.gov/qcalc/
41. National Institute of Standards and Technology. (2017). Stopping-Power and Range Tables for Protons. Retrieved May 2022 from https://physics.nist.gov/PhysRefData/Star/Text/PSTAR.html
42. International Atomic Energy Agency. (2022). Evaluated Nuclear Data File Database. Retrieved May 2022 from https://www-nds.iaea.org/exfor/endf.htm
43. Richardson RB, Harper ME. Mitochondrial stress controls the radiosensitivity of the oxygen effect: implications for radiotherapy. Oncotarget 2016; 7:21469–83.
44. Rolfe DF, Hulbert AJ, Brand MD. Characteristics of mitochondrial proton leak and control of oxidative phosphorylation in the major oxygen-consuming tissues of the rat. Biochim Biophys Acta 1994; 1188(3):405–16.
45. Nguyen AM, Rao NA. Oxidative photoreceptor cell damage in autoimmune uveitis. J Ophthalmic Inflamm Infect 2011; 1:7–13.
46. da Silveira WA, Fazelinia H, Rosenthal SB, Laiakis EC, Kim MS, Meydan C, et al. Comprehensive multi-omics analysis reveals mitochondrial stress as a central biological hub for spaceflight impact. Cell 2020; 183:1185–201 e20.
47. Mao XW, Boerma M, Rodriguez D, Campbell-Beachler M, Jones T, Stanbouly S, et al. Acute effect of low-dose space radiation on mouse retina and retinal endothelial cells. Radiat Res 2018; 190: 45–52.
48. Beebe DC, Holekamp NM, Shui YB. Oxidative damage and the prevention of age-related cataracts. Ophthalmic Res 2010; 44(3): 155–65.
49. Holekamp NM, Shui YB, Beebe D. Lower intraocular oxygen tension in diabetic patients: possible contribution to decreased incidence of nuclear sclerotic cataract. Am J Ophthalmol 2006; 141(6):1027–32.
50. Hayashi T, Kusunoki Y, Hakoda M, Morishita Y, Kubo Y, Maki M, et al. Radiation dose-dependent increases in inflammatory response markers in A-bomb survivors. Int J Rad Biol 2003; 79(2):129–36.
51. Eltzschig HK, Bratton DL, Colgan SP. Targeting hypoxia signalling for the treatment of ischaemic and inflammatory diseases. Nat Rev Drug Discov 2014; 13(11):852–69.
52. Loganovsky KN, Marazziti D, Fedirko PA, Kuts KV, Antypchuk KY, Perchuk IV, et al. Radiation-induced cerebro-ophthalmic effects in humans. Life (Basel) 2020; 10(4):41.
53. ICRP 74, Conversion Coefficients for use in Radiological Protection against External Radiation. Ann ICRP 1996; 26:1–205.
54. ICRP 116, Conversion Coefficients for Radiological Protection Quantities for External Radiation Exposures. Ann ICRP 2010; 40: 1–257.
55. ICRP 119, Compendium of Dose Coefficients based on ICRP Publicaiton 60. Ann ICRP 2012; 41:1–130.
56. Paliwal B, Tewatia D. Advances in radiation therapy dosimetry. J Med Phys 2009; 34(3):108–16.
57. Health Canada. (2020). National Dosimetry Services (NDS) products. Retrieved April 2023 from https://www.canada.ca/en/health-canada/services/dosimetry/products.html
58. Dubeau J, Sun J, Djeffal S, Leroux N, Golovko V, Dodkin C, Mistry R. Current status of eye-lens dosimetry in Canada. J Radiol Prot 2022; 42(1):011520.
59. Gualdrini G, Ferrari P, Tanner, R. Fluence to $H_p(3)$ conversion coefficients for neutrons from thermal to 15 MeV. Radiat Prot Dosim 2013; 157(2); 278–90.
60. Clairand I, Behrens R, Brodecki M, Carinou E, Domienik-Andrzejewska J, Ginjaume M, Hupe O, Roig M. EURADOS 2016 Intercomparison Exercise of Eye Lens Dosemeters. Radiat Prot Dosim 2018; 182(3):317–22.

61. Dubeau J, Sun J, Leroux N, Atanackovic J, Dauer LT, Hakmana Witharana SS, Hanu A. A study on the use of modified extremity dosemeters for the measurement of $H_p(3,\alpha)$. Radiat Meas 2021; 140:106491.

62. Hatami A, Bagheri M, Falahati F, Banaei A, Abedi-Firouzjah R, Zamani H, Kiapour M, Momeni F. Estimating the whole-body effective dose and health risks as well as introducing a new easy method for eye lens dosimetry in interventional cardiology procedures. MethodsX 2020; 7:101097.

63. Miyaji N, Miwa K, Iimori T, Wagatsuma K, Tsushima H, Yokotsuka N, Murata T, Kasahara T, Terauchi T. Determination of a reliable assessment for occupational eye lens dose in nuclear medicine. J Appl Clin Med Phys 2022; 23(8):1–10.

64. Siebert BRL, Schuhmacher, H. Quality factors, ambient and personal dose equivalent for neutrons, based on the new ICRU stopping power data for protons and alpha particles. Radiat Prot Dosim 1995; 58(3):177–183.

65. El Basha D, Furuta T, Iyer S S R, Bolch W E. A scalable and deformable stylized model of the adult human eye for radiation dose assessment. Phys Med Biol 2018; 63(10):105017.

66. An MCNP Primer. Manhattan, Kansas: Kansas State University; 2011. (https://www.mne.k-state.edu/~jks/MCNPprmr.pdf)